

Stratification governs the Existence of Surface-Intensified Eastward Jets in Turbulent Gyres without Bottom Friction

LENNARD MILLER,^{a,b}, BRUNO DEREMBLE^b, ANTOINE VENAILLE^a

^a *ENS de Lyon, CNRS, Laboratoire de Physique (UMR CNRS 5672), F-69342 Lyon, France*

^b *Université Grenoble Alpes, CNRS, INRAE, IRD, Grenoble-INP, Institut des Géosciences de l'Environnement, Grenoble, France*

ABSTRACT: This study examines the role of stratification in the formation and persistence of eastward jets (like the Gulf Stream and Kuroshio currents). Using a wind-driven, two-layer quasi-geostrophic model in a double-gyre configuration, we construct a phase diagram to classify flow regimes. The parameter space is defined by a criticality parameter ξ , which controls the emergence of baroclinic instability, and the ratio of layer depths δ , which describes the surface intensification of stratification. Eastward jets detaching from the western boundary are observed when $\delta \ll 1$ and $\xi \sim 1$, representing a regime transition from a vortex-dominated western boundary current to a zonostrophic regime characterized by multiple eastward jets. Remarkably, these surface-intensified patterns emerge without considering bottom friction. The emergence of the coherent eastward jet is further addressed with complementary 1.5-layer simulations and explained through both linear stability analysis and turbulence phenomenology. In particular, we show that coherent eastward jets emerge when the western boundary layer is stable, and find that the asymmetry in the baroclinic instability of eastward and westward flows plays a central role in the persistence of eastward jets, while contributing to the disintegration of westward jets.

SIGNIFICANCE STATEMENT: Eastward oceanic jets at mid-latitudes, such as the Gulf Stream or the Kuroshio, are important in oceanic circulation as they transport water masses from western boundary currents far into the open ocean. This study uses an idealized model to isolate the role of density stratification on the formation of such jets in turbulent gyres. Our findings describe density profiles that are favourable for jet formation and highlight the importance of strong stratification close to the surface.

1. Introduction

Surface-intensified eastward jets detaching from western boundaries are a prominent feature of mid-latitude oceans. Two iconic examples are the Gulf Stream and the Kuroshio, which appear as coherent, narrow, meandering ribbons surrounded by mesoscale oceanic rings in snapshots of surface kinetic energy (Chassignet and Xu 2021). Satellite altimetry and state-estimate reconstructions show that these jets often maintain a coherent structure over long distances (Forget et al. 2015), despite the transition from coastal to open-ocean environments (Chassignet and Marshall 2008). Coherent eastward jets are also found across a wide range of models, from high-resolution primitive equation models (Ajayi et al. 2020) to simple two-layer quasi-geostrophic models (Holland 1978; Berloff and McWilliams 1999a). In spite of its robustness, a simple theoretical description of the eastward jet in turbulent, western-intensified gyres is still lacking.

Eastward jets in quasi-geostrophic gyres have attracted significant attention over the last few decades. One approach, based on dynamical system theory, begins with viscous solutions (Stommel 1948; Munk 1950) and examines successive bifurcations as dissipation is reduced (Veronis 1966; Cessi and Ierley 1995; Dijkstra and Ghil 2005). In this context, Simonnet (2005) described a weakly time-dependent eastward jet controlled by dissipative mechanisms in a one-layer quasi-geostrophic model. However, reaching sufficiently low dissipation regimes relevant to the real ocean remains a challenging task, as it leads to the excitation of an increasing number of degrees of freedom. A complementary theoretical approach has focused on constructing solutions for zones of inertial recirculation when the boundary layer approximation breaks down (Cessi et al. 1987; Ierley 1990). Nakano et al. (2008) outlined a solution where an eastward jet flanked by inertial recirculation reconnects to a Sverdrup interior, but emphasize the difficulty of correctly describing the dynamical balance of the recirculation zones. Both their stability and driving mechanisms (Holland and Schmitz 1985; Sun et al. 2013) pose a tenacious problem for the closure of mathematical models describing such inertial recirculation embedded in turbulent gyres (Kubokawa 2023).

In the limit of vanishing viscosity, equilibrium statistical mechanics has been employed to predict the self-organization of ocean currents on basin scales. On the beta plane, at low energy, equilibrium statistical mechanics consistently yields Fofonoff flows (Salmon et al. 1976; Bretherton and Haidvogel 1976). These solutions are characterized by strong jets, but these jets are westward

Corresponding author: Lennard Miller, lennard.miller@ens-lyon.fr

and confined only to the boundaries. At sufficiently higher energy levels, 1.5-layer quasi-geostrophic models with a small Rossby radius of deformation predict the formation of intense zonal jets in the interior, separating regions of homogenized vorticity (Venaille and Bouchet 2011). While these inviscid approaches can lead to meaningful descriptions of inertial recirculation regions (Marshall and Nurser 1986), they fail to account for western intensification when applied at the scale of an ocean basin. To wit, ocean gyres are strongly out of equilibrium turbulent systems.

A challenging aspect of mesoscale turbulence in ocean gyres is its propensity to rectify the large-scale flow that initiated small-scale motion through instabilities. In that context, baroclinic turbulence has often been addressed by looking at the equilibration of quasi-geostrophic fluctuations around a prescribed unstable mean flow in doubly periodic domains (Salmon 1998; Arbic and Flierl 2004b). This "local" perspective has helped interpret observed flow patterns, such as vortices and meandering jets, based on the observed local mean flow in different regions of the ocean (Venaille et al. 2011), and it has also lead to the design of useful parameterizations of baroclinic turbulence in coarser models (Gallet and Ferrari 2020; Hadjerci and Gallet 2023, 2024). Among the variety of reported baroclinic turbulent regimes (Arbic and Flierl 2004a), formation of coherent jets have been described (Arbic and Flierl 2003; Venaille et al. 2014). While these patterns share similarities with Gulf Stream or Kuroshio jets they were only found in the limit of large bottom friction, which is not relevant for the ocean. Moreover, the locality assumption behind studies in doubly periodic geometries has been strongly questioned (Grooms et al. 2013). Thus, a minimal model for coherent eastward jets must account for non-local processes and move beyond the large friction assumption.

The main goal of the present work is to isolate the role of stratification in oceanic jet formation. Therefore we employ a quasi-geostrophic model of mid-latitude gyres and consider a scenario without bottom friction. Although bottom friction is needed to stabilize the energy cycle of unbounded geostrophic turbulence (Salmon 1998), a significant amount of energy is supposed to be dissipated by flow-topography interactions close to the western boundary in more realistic settings (Dewar and Hogg 2010; Molemaker et al. 2015; Deremble et al. 2017). We aim to reproduce this so-called "western eddy-graveyard" (Zhai et al. 2010; Yang et al. 2021) by applying no-slip boundary conditions, which may act as an efficient energy sink while remaining in a quasi-geostrophic modelling framework (Miller et al. 2024).

The structure of the article is as follows: In section 2, we describe the two-layer model and introduce the reduced parameter space which describes the vertical stratification properties. In section 3, we use numerical simulations to identify three distinct stratification regimes: strong, intermediate, and weak. We then shift our attention to the intermediate stratification regime. Section 4 presents a local linear stability analysis of surface-intensified gyres, paying particular attention to the distinct stability characteristics of the eastward and westward parts of the gyres, as well as the western boundary layer. In section 5, we explore the inviscid mechanisms behind the formation of zonally penetrating jets. We compare a two-layer and a one-and-a-half-layer quasi-geostrophic simulations to identify the dynamics specifically linked to baroclinic instability. Finally, in section 6, we discuss the transition to a zonostrophic regime, which precedes the weak stratification regime characterized by barotropic gyres. We conclude in section 7 by outlining the minimal conditions required for the emergence and persistence of a coherent jet between the gyres.

2. Flow Model

The simplest model to address the effect of stratification on wind-driven circulation consists of two layers of fluid following quasi-geostrophic motion, considered here in a double-gyre configuration. The equations of evolution of the upper layer and lower layer potential vorticity (q_1 and q_2) are

$$\frac{\partial q_1}{\partial t} + \mathbf{u}_1 \cdot \nabla q_1 = \frac{\nabla \times \boldsymbol{\tau}}{H_1} + \nu \nabla^4 \psi_1 \quad (1)$$

$$\frac{\partial q_2}{\partial t} + \mathbf{u}_2 \cdot \nabla q_2 = \nu \nabla^4 \psi_2 \quad (2)$$

$$q_1 = \nabla^2 \psi_1 + \frac{1 - \delta}{L_d^2} (\psi_2 - \psi_1) + \beta y \quad (3)$$

$$q_2 = \nabla^2 \psi_2 + \frac{\delta}{L_d^2} (\psi_1 - \psi_2) + \beta y \quad (4)$$

with ψ_i the streamfunction and $\mathbf{u}_i = (u_i, v_i) = (-\partial_y \psi_i, \partial_x \psi_i)$ the velocity in each layer. We solve this system of equations on a square domain with $(x, y) \in [0, L]^2$, and apply no-slip boundary conditions.

The forcing $\boldsymbol{\tau} = (\tau_0 \sin(2\pi y/L), 0)$ models a classical double gyre. Stratification is completely described by the relative upper layer thickness and the first baroclinic Rossby radius of deformation, defined respectively as

$$\delta = \frac{H_1}{H_1 + H_2}, \quad L_d = \sqrt{\frac{g' H_1 H_2}{(H_1 + H_2) f_0^2}}, \quad (5)$$

with g' being the reduced gravity between both layers and f_0 the Coriolis parameter. In addition to δ , the problem admits three non-dimensional parameters:

$$\tilde{\nu} = \frac{\nu}{U_{Sv}L}, \quad \tilde{\beta} = \frac{\beta L^2}{U_{Sv}}, \quad \xi = \frac{U_{Sv}}{\beta L_d^2}, \quad (6)$$

with

$$U_{Sv} = \frac{8\pi\tau_0}{H_1L\beta}. \quad (7)$$

The velocity U_{Sv} gives the order of magnitude of the zonal flow in the gyres when circulation is confined in the upper layer and is set to $U_{Sv} = 0.09 \text{ ms}^{-1}$ in all simulations. The parameters $\tilde{\nu}$ and $\tilde{\beta}$ are also kept constant throughout this study, such that the thickness of the inertial boundary layer is always $\delta_I = L/\sqrt{\tilde{\beta}} = 72 \text{ km}$ (Charney (1955)) and the viscous sublayer is always $\delta_P = L\sqrt{\tilde{\nu}/\sqrt{\tilde{\beta}}} = 3 \text{ km}$ (Pedlosky 1987; Ierley and Ruehr 1986) for a basin of size $L = 4000 \text{ km}$. We will focus on examining the dynamical regimes that appear upon varying the two parameters ξ and δ .

The parameter δ is a proxy for surface-intensified stratification, but small values of δ do not always imply surface-intensified currents as the system may adjust to settle into a barotropic state. The parameter ξ is sometimes called the criticality parameter, related to baroclinic instability (Held and Larichev 1996; Jansen and Ferrari 2012). In order to reach asymptotic behaviour, we vary ξ from 10^{-2} to 10^2 for $\delta = 0.5$, from 1 to 5.6 for $\delta = 1/6$ and from 10^{-1} to 10^3 for $\delta = 0.01$. This corresponds to changing L_d from 737 km to 7 km, 72 km to 13 km and 233 km to 2 km, respectively. In our numerical simulations, we change L_d by setting g' , which controls ξ but leaves all other non-dimensional variables unchanged. A summary of the dimensional variables of the simulations is given in table 1.

To numerically solve equations (1) - (4) the code *qgw* was used. It uses classical finite differences discretization of the equations with an Arakawa formulation of the Jacobian and a direct spectral inversion (after projection on the vertical modes) to obtain the streamfunction ψ from the potential vorticity q . Time stepping is done with an adaptive 2nd order Adams-Bashforth technique, where the time step is determined by a standard CFL-condition.

Unless specified, all runs are performed with 4096×4096 grid points on the horizontal, corresponding to a resolution of 1 km, ensuring all relevant flow scales of the problem are well resolved. We paid attention to run the simulations for at least two gyre turnover times $T_{Gyre} = L/U_{Sv}$ after the spinup was completed. Last, the no-slip boundary condition is implemented as in Miller et al. (2024).

TABLE 1. Parameters of the 2-layer Model for Wind-driven Oceanic Circulation.

Name	Variable	Values in Simulations
Upper Layer Depth	H_1	2000 m, 666 m, 40 m
Lower Layer Depth	H_2	2000 m, 3334 m, 3960 m
Domain size	L	4000 km
Beta	β	$1.7 \times 10^{-11} \text{ m}^{-1} \text{ s}^{-1}$
Viscosity	ν	$10 \text{ m}^2 \text{ s}^{-1}$
Deformation Radius	L_d	2.3 km, ..., 720 km $50 \times 10^{-5} \text{ m}^2 \text{ s}^{-2}$,
Wind Stress	τ_0	$16 \times 10^{-5} \text{ m}^2 \text{ s}^{-2}$, $1 \times 10^{-5} \text{ m}^2 \text{ s}^{-2}$

3. Numerical Simulations

a. Reference Run

A reference run displaying an eastward jet detaching from the western boundary is shown in figure 1, where the barred quantities denote time-averages. The criticality and layer aspect ratio are set to $(\xi, \delta) = (3.3, 0.01)$, corresponding to a deformation radius $L_d = 40 \text{ km}$. The flow is western- and surface-intensified in both instantaneous and time-averaged fields, and total transport scales well with the Sverdrup scaling $\psi_{Sv} = U_{Sv}L/4$. The upper-layer potential vorticity is nearly homogenized around values of ψ_{Sv}/L_d^2 in each gyre, with the potential vorticity jump at the interface between the two gyres corresponding to an eastward jet. In instantaneous kinetic energy snapshots, this jet appears with a thickness close to L_d and sheds blobs of potential vorticity that have opposite signs of potential vorticity to the background, similar to Gulf stream rings (Kurashina et al. 2021)). Our aim in this article is to explain how and when stratification renders such states possible in double-gyre configurations without bottom friction.

b. Parameter Space

In order to understand the robustness of eastward jets detaching from western boundaries we now explore a broader stratification parameter range by spanning the parameter space (ξ, δ) , focusing on the asymptotic values of $\delta = 0.5$ and $\delta = 0.01$. This parameter space, displayed in figure 2, is dissected into a strong stratification regime when $\xi < 1$, a weak stratification regime when $1/\delta < \xi$, and an intermediate stratification regime in between. As detailed in the next section, the transitions at $\xi = 1$ and $\xi = 1/\delta$ correspond to the onset of baroclinic instability for westward flow and eastward flows, respectively. The line $\xi = 1/\delta$ also corresponds to the onset of barotropization of the Sverdrup gyres, according to classical theory of potential

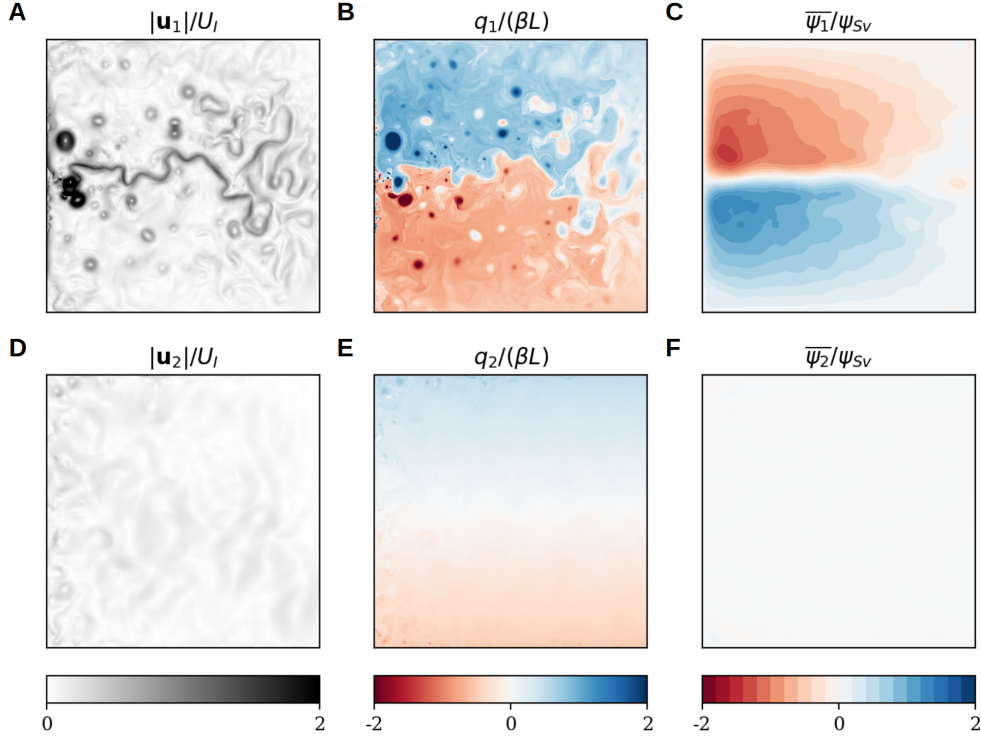


FIG. 1. Upper layer (top row) and lower layer (bottom row) for the reference run at $\delta = 0.01$, $\xi = 10$. (A, D) Flow speed $|\mathbf{u}_i|$ normalized with inertial velocity $U_I = \psi_{Sv}/\delta l$, (B, E) potential vorticity normalised by planetary vorticity and (C, F) time-mean streamfunction normalised by Sverdrup scaling.

vorticity homogenization in planetary gyres (Rhines and Young (1982), see also appendix B). To measure surface intensification of the large-scale velocity field we compute the ratio

$$B = \frac{|u_1^{proj}|}{|u_1^{proj}| + |u_2^{proj}|} \quad (8)$$

with

$$u_i^{proj} = \frac{2}{L^2} \iint \bar{u}_i \cos\left(\frac{2\pi y}{L}\right) dx dy, \quad (9)$$

shown in figure 3. The projection on the gravest meridional mode is used to remove rectified zonal structures (Fox-Kemper 2004; Nadiga and Straub 2010), and we use the time-averaged zonal velocity \bar{u}_i in order to weaken the imprint of western boundary currents not accounted for in classical theory (Rhines and Young 1982). B decreases from 1, corresponding to a complete surface intensification, to 0.5, corresponding to an equality between surface and lower layer velocities, which we define here as the barotropic state.

In the strong stratification regime ($\xi < 1$), gyres remain confined to the upper layer, but Gulf Stream-like jets are not observed. Instead, instantaneous fields display strong vortices generated through the detachment of the viscous

sublayer at the western boundary (not shown). This regime corresponds to Gyre Turbulence as reported on in Miller et al. (2024), except that the finite value of L_d in the present case tends to stabilize an intense vortex dipole close to the western boundary. The time-averaged bulk structures are similar for both values of δ and resembles a Sverdrup gyre, albeit with notable rectification (figure 2, left panels). Although we filter the signal, these rectified barotropic gyres at $\delta = 0.5$ which form close to the meridional boundaries correspond to B less than 1 due to their projection on the gravest meridional mode (figure 3A), but in fact all Sverdrup transport remains confined in the upper layer. We attribute the rectification to the presence of barotropic basin modes which can energize the lower layer when $\delta \sim 1$ (figure 3B), but expect a complete decoupling between the two layers in the limit of an infinite Rossby radius of deformation (corresponding to $\xi \rightarrow 0$) regardless of the value of δ .

In the weak stratification regime ($\xi > 1/\delta$) the gyres become increasingly barotropic, as measured by B (figure 3A). The flow at $\delta = 0.5$ closely resembles the barotropic Gyre Turbulence regime observed by Miller et al. (2024). This barotropization is visible in the collapse of upper and lower layer kinetic energies and

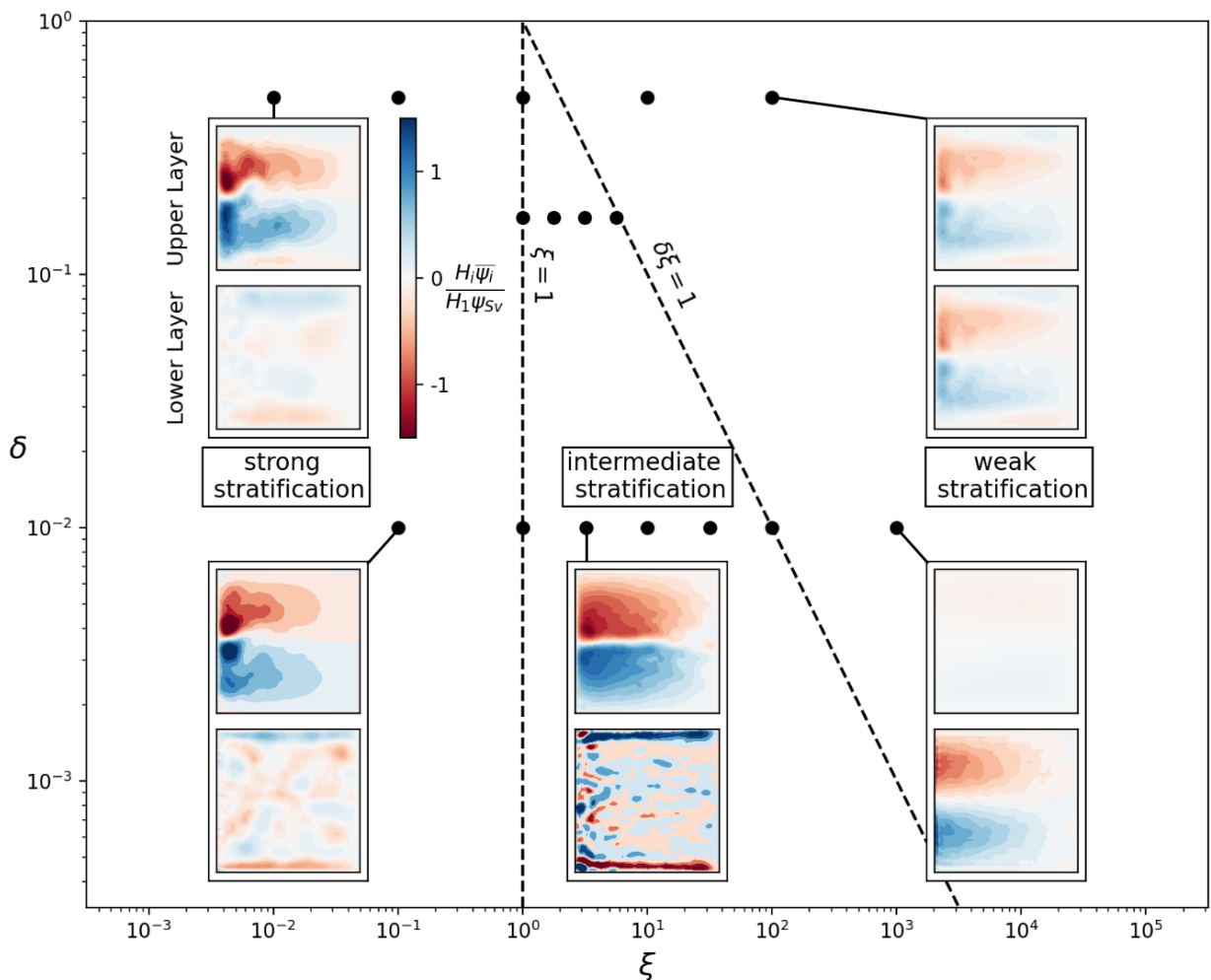


Fig. 2. Parameter space spanned by ξ and δ . The vertical line at $\xi = 1$ marks the onset of baroclinic instability, while the slanted line $\delta \xi = 1$ signifies the barotropization of a Sverdrup flow. Black dots mark simulation parameters. The insets show the time-mean vertically integrated transport in the upper and lower layer for example runs of each regime. The colorscale is normalized by the Sverdrup transport $\psi_{Sv} = U_{Sv}L/4$.

in the decrease of the index B . For $\delta = 0.01$ the flow enters the weak stratification regime when $\xi > 100$, and the transition is less abrupt than for $\delta = 0.5$. The time-averaged barotropic gyres align more closely with Sverdrup balance, visible in the decline of B (also in the bottom right panel of figure 2). We find large areas of homogenized potential vorticity in the lower layer for both $\delta = 0.5$ and $\delta = 0.01$. However, the upper layer flow is no longer in Sverdrup balance but instead shows a loss of western intensification. For further details on the weak stratification regime and potential vorticity homogenization the reader is referred to appendix B.

The focus of this manuscript lies on the intermediate stratification regime, due to the appearance of eastward jets in gyres such as presented in the reference run. This

regime is characterised by $1 < \xi < 1/\delta$ and is hence accessible only when $\delta \ll 1$. We therefore focus on the runs at $\delta = 0.01$, limiting our description to the upper layer as the dynamics remain mostly surface-intensified (figure 3). The surface flow pattern are displayed in figure 4. As ξ is increased, a continuous transition occurs from western-intensified gyres to a state that restores east-west symmetry, with a decrease in total transport of the gyres. Coincidentally, the dominant turbulent flow features change. The strong coherent vortices which dominate the flow in the strong stratification regime disappear, and instead a sea of eddies of characteristic size L_d develops in the regions of westward flow. In the regions of eastward flow, the transition is marked by the emergence of strong jets, initially as a single jet ($1 \lesssim \xi \lesssim 10$) and later as multiple jets associated with

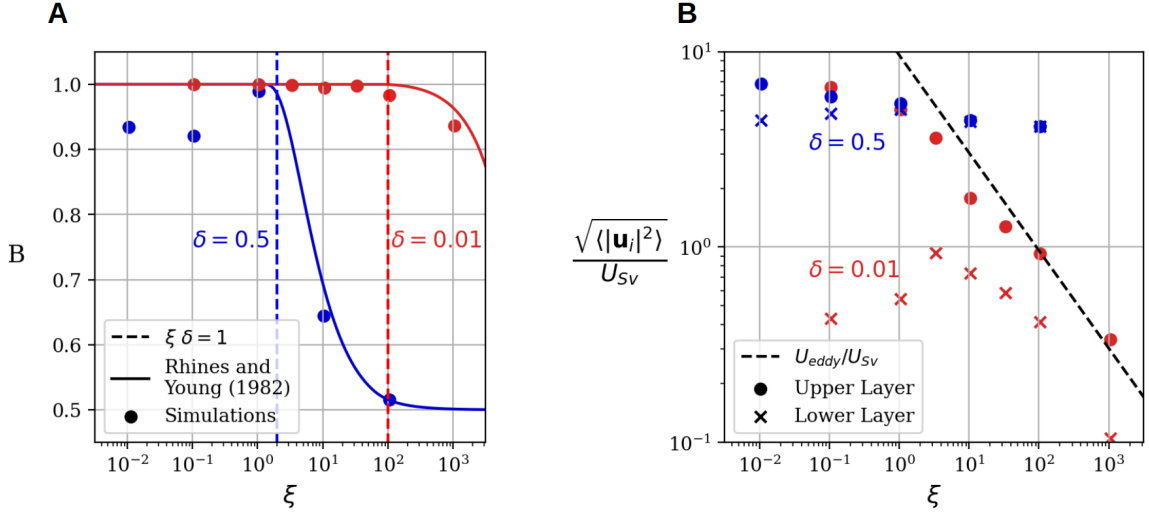


FIG. 3. (A) Barotropization measure B of the mean Sverdrup flow as defined in equation (8), and (B) root mean square velocity as a function of ξ . For details on the predictions of homogenization theory from Rhines and Young (1982) in A the reader is referred to appendix B.

potential vorticity staircases ($10 \lesssim \xi$).

The runs which were performed at $\delta = 1/6$ are omitted in the main text as no eastward jet was observed in this case. Its absence is interpreted as a result of the energetic vortex gas that forms at low viscosity when no-slip boundary conditions are applied (Miller et al. 2024). Further details on these runs can be found in appendix A.

In the remainder of this paper, we use a combination of linear stability analysis, scaling analysis and complementary simulations to rationalize the transition occurring in the intermediate stratification regime at $\delta = 0.01$ (figure 4), rationalizing both the emergence and disappearance of the eastward jet detaching from the western boundary.

4. Linear Stability Analysis

Here, we provide a linear stability analysis of the mean flow associated with surface-intensified gyres and inertial western boundary layers. This analysis will help interpreting the parameter space laid out in the previous section. To simplify, we consider two sub-problems:

- A horizontally homogeneous eastward or westward flow confined to the upper layer, with prescribed magnitude U_{Sv} .
- A meridional velocity profile typical of inertial western boundary currents. This velocity profile varies in

the x -direction over a scale of δ_l and is invariant in the y -direction.

The first case is the textbook Phillips problem for baroclinic instability on the beta plane (Vallis 2017). Similar cases to the second one can be found in Ierley and Young (1991) and Berloff and McWilliams (1999b). Here, we present only the key results relevant for interpreting the nonlinear simulations in the parameter space (ξ, δ) . For more details, the reader may consult appendix C.

Baroclinic instability in the Phillips model on the beta-plane is known to be asymmetric with respect to the zonal direction of the base flow (Pedlosky 1987). This asymmetry is illustrated in figure 5, which shows the maximum growth rate as a function of δ and ξ for both eastward and westward flows. The asymmetry appears in the intermediate stratification regime: westward flow becomes unstable for $\xi > 1$, while eastward flow becomes unstable for $\xi > 1/\delta$. The eastward flow in the gyres is hence expected to remain baroclinically stable in the intermediate stratification regime, while the westward flow of the gyres is baroclinically unstable. In the weak stratification regime, where surface-intensified flow in both directions is unstable, Sverdrup flow becomes barotropic according to potential vorticity homogenization theory, thus invalidating our initial hypothesis of a surface-intensified gyre.

We also conducted a linear instability analysis of the western boundary layer, as shown in figure 6. The base

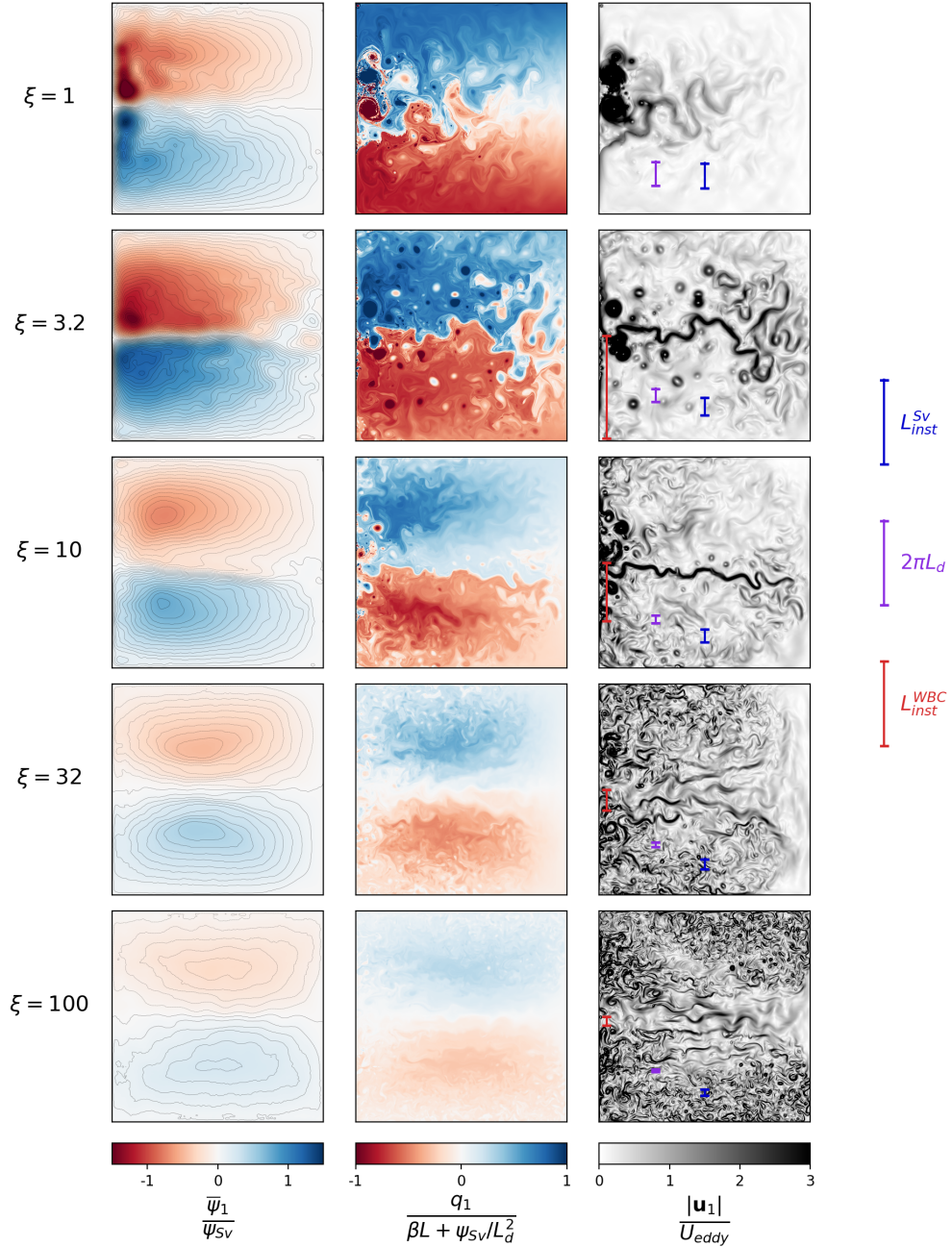


FIG. 4. Time-average of ψ_1 (left column) and snapshots of q_1 (middle column) and $|\mathbf{u}_1|$ (right column) for simulations in the intermediate stratification regime at $\delta = 0.01$. The stream functions are normalized by the Sverdrup scale ψ_{Sv} and contour intervals are 0.05. q_1 is normalized by the planetary geostrophic vorticity of Sverdrup flow $(\beta L + \psi_{Sv}/L_d^2)$ and the velocity scale U_{eddy} is given in equation (13). The brackets shown on the right allow to compare the instability scales of the western boundary current L_{inst}^{WBC} and of the interior Sverdrup flow L_{inst}^{Sv} to L_d .

profile of the meridional velocity, depicted in figure 6A, is assumed to be

$$v = U_I(e^{-\frac{x}{\delta_I}} - e^{-\frac{x}{\delta_P}}). \quad (10)$$

It follows an exponential function with a decay rate determined by the inertial layer thickness δ_I . Additionally, a viscous sublayer is modeled by including another exponential term with a decay rate of δ_P , bringing the velocity to zero near the western boundary. The

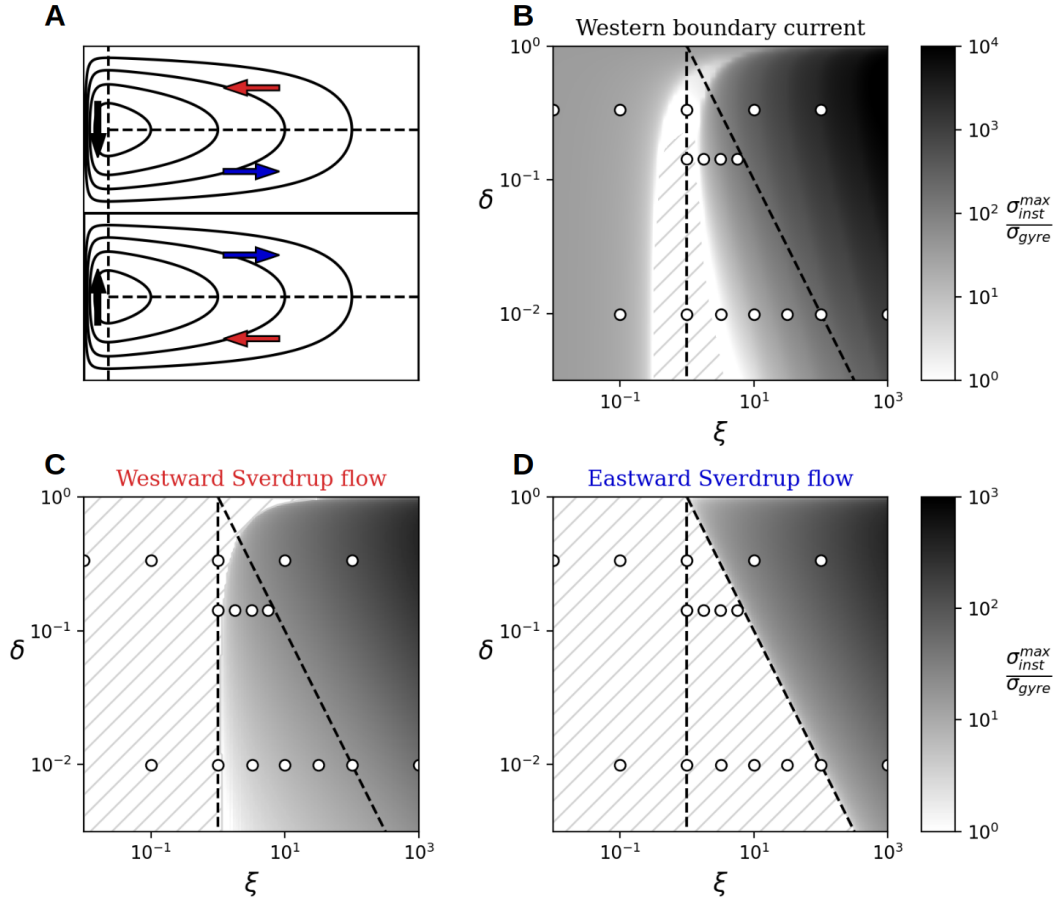


FIG. 5. Results of linear stability analysis of interior Sverdrup flow with an inertial western boundary current. (A) Schematic of the reprinted regions, and maximum growth rates for (B) western boundary currents, (C) westward Sverdrup flow and (D) eastward Sverdrup flow. The system is stable in the hatched regions. In the unstable domain, the growth rate (black shading) is rescaled by the gyre turnover rate, $\sigma_{gyre} = U_{Sv}/L$, and the colorbar for eastward flow applies for westward flow, too.

velocity amplitude is determined by the inertial velocity $U_I = \psi_{Sv}/\delta_I$, ensuring that the gyre's transport fully recirculates within this boundary layer profile. Further details can be found in Appendix C. The growth rate of the most unstable mode in this case is plotted as a function of (ξ, δ) in figure 5B and in figure 6B for the case $\delta = 0.01$. An important result of this analysis is the existence of a stability island around $\xi = 1$ for sufficiently small δ . Near $\xi = 1$, the western boundary stabilizes the meridional flow which should otherwise be baroclinically unstable (Spall 2000). In figure 6B, we also plot the growth rate of the most unstable mode for the same velocity profile in a 1.5-layer quasi-geostrophic model, obtained by assuming $\psi_2 = 0$. This demonstrates that instabilities at $\xi < 1$ are due to horizontal shear instabilities of the boundary layer, while instabilities at larger criticality parameters are genuinely baroclinic, as they are absent in the 1.5-layer

model.

In figure 4 (right panels), we plot the wavelength of the most unstable mode for both the western meridional flow and the interior zonal flow, to compare this length scale with flow structures. For the interior flow, the most unstable mode has a length scale $2\pi L_d$, which appears to qualitatively match the size of the vortex rings. In contrast, for the western boundary current, the instability scale is initially much larger than the deformation radius, and only at values of $\xi > 10$ approaches the order of the deformation radius. Snapshots of ψ show the presence of large-scale basin modes (not shown), which may result from this instability at intermediate $\xi \sim 10$. At higher $\xi \sim 100$, baroclinic instability is supposedly of the same type as in the interior flow, as the instability scale becomes much smaller than the scale of the base

profile, δ_I . However, at this point the mean flow is no longer western intensified (figure 4A). Baroclinic instability itself may in fact be responsible for this erosion of Sverdrup flow, but a detailed analysis of the mean flow balance is beyond the scope of the present work.

5. The Eastward Jet ($1 \lesssim \xi \lesssim 10$): Insights from the 1.5-Layer Model

To disentangle the role of baroclinic instability and intrinsic surface layer dynamics in the emergence of the eastward jet we performed a set of 1.5-layer numerical simulations, assuming $\psi_2 = 0$ at all times in equation (4) with all other parameters kept identical. A comparison between the two-layer model and the 1.5-layer model is shown with plots of the instantaneous speed in figure 7.

In the strong stratification regime ($\xi < 1$), both models yield a similar flow pattern, resembling the Gyre Turbulence regime of Miller et al. (2024). This suggests that the dynamics are primarily governed by 1.5-layer dynamics, consistent with the linear computation predicting no baroclinic instability in this parameter range. As ξ becomes larger than one, both models simulate a change of regime with the emergence of strong eastward jets. However, a notable difference occurs: recirculating westward jets appear in the 1.5-layer model but not in the two-layer model (see figure 7B and figure 7E). We argue that the mechanism for the apparition of the eastward jet is the same in both models, but that baroclinic instability of the westward jets is responsible for their absence in the two-layer model.

To interpret the emergence of the eastward jet, we focus on the transition observed in the 1.5-layer model and propose two complementary perspectives based on turbulence phenomenology in unbounded geometry and western boundary layer dynamics.

First, we note that the transition from a gas of isolated vortices to jet-like structures is a common occurrence in stratified two-dimensional turbulence (Bouchet and Venaille 2012; Venaille et al. 2015; Frishman et al. 2017). In the specific case of unbounded isotropic 1.5-layer turbulence, it has long been observed that injecting energy at scales much smaller than the Rossby radius of deformation leads to isolated vortices, sometimes organized into vortex crystals (Kukharkin et al. 1995). In contrast, injecting energy at scales larger than the Rossby radius of deformation results in the formation of large-scale potential vorticity staircases (Arbic and Flierl 2003; Burgess and Dritschel 2022). By definition of potential vorticity, the interfaces of these staircases are associated with sharp jets of width L_d : these are the

meandering ribbons, which share strong similarities with the eastward jet detaching from the western boundary. A physical interpretation for the emergence of such potential vorticity staircases has been proposed as the most probable outcome of turbulent potential vorticity mixing (Venaille et al. 2014).

These previous studies suggest that the key parameter governing the transition from a vortex gas to Gulf Stream-like jets is the ratio of the energy injection length scale to the Rossby radius of deformation. In the vortex gas regime, the inertial boundary layer thickness δ_I sets the maximum scale of the eddies injected from the boundary into the bulk, eventually leading to a vortex gas (Miller et al. 2024). This suggests that the transition from a vortex gas to ribbon states is governed by $\delta_I/L_d = \sqrt{\xi}$, which is consistent with the transition occurring at $\xi = 1$.

The presence of β and impermeable boundaries in our simulation may change details of this turbulence-driven transition. We note that isolated vortices drift westward at a speed of βL_d^2 , and that the vortex gas regime depends on the ability of these vortices to efficiently interact with the western wall. This interaction is prevented in the eastward parts of the gyres when $U_{sv} > \beta L_d^2$, which again amounts to $\xi > 1$. Thus, the condition for the existence of the vortex gas regime is also consistent with the observed transition at $\xi = 1$.

So far, we have explained how turbulence may drive a change in the flow pattern within the domain bulk. We now discuss how these patterns may be connected with changes in the western boundary layer dynamics. The emergence of the eastward jet roughly coincides with the stabilization of the western boundary layer (Figure 5), and we hypothesize this stability to give rise to similar recirculation zones as observed in free-slip solutions (Ierley and Young 1988). Excitation of different inertial recirculation modes, as outlined by Marshall and Marshall (1992), might also be relevant during the transition. In the asymptotic limits, the 1.5-layer solutions are characterised by tight, modon-like recirculation when $\xi \ll 1$ (mean flow not shown, but similar to left panels of figure 2) and by Fofonoff flow when $\xi \gg 1$, resembling inertial runaway (Sheremet et al. (1995), figure 7F). However, when $\xi \sim 1$, both a strong modon and a penetrating jet are present in the outflow region of the western boundary layer (figure 7E), and discussing the flow in terms of stationary inertial solutions only does not seem adequate. Although a mechanism setting the pattern of inertial recirculation is left to be identified, these runs are readily compared to the 2-layer simulations. Intense westward parts of inertial recirculation disappear in the 2-layer runs (7B), which is attributed to zonal asymmetry of baroclinic instability in

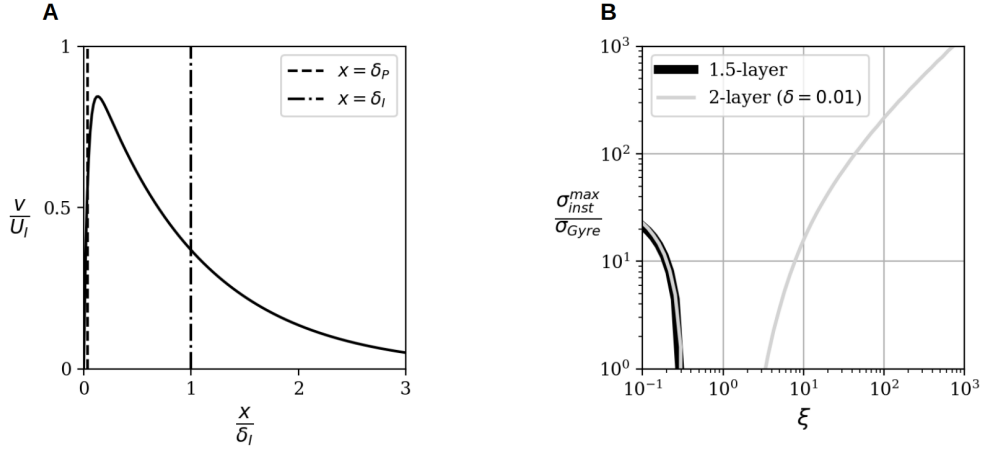


FIG. 6. (A) Base velocity profile for the linear stability analysis of the inertial western boundary layer and (B) comparison of growth rates in the 1.5-layer model and the 2-layer model. The unstable branch at $\xi > 1$ visible in the 2-layer model only is attributed to baroclinic instability.

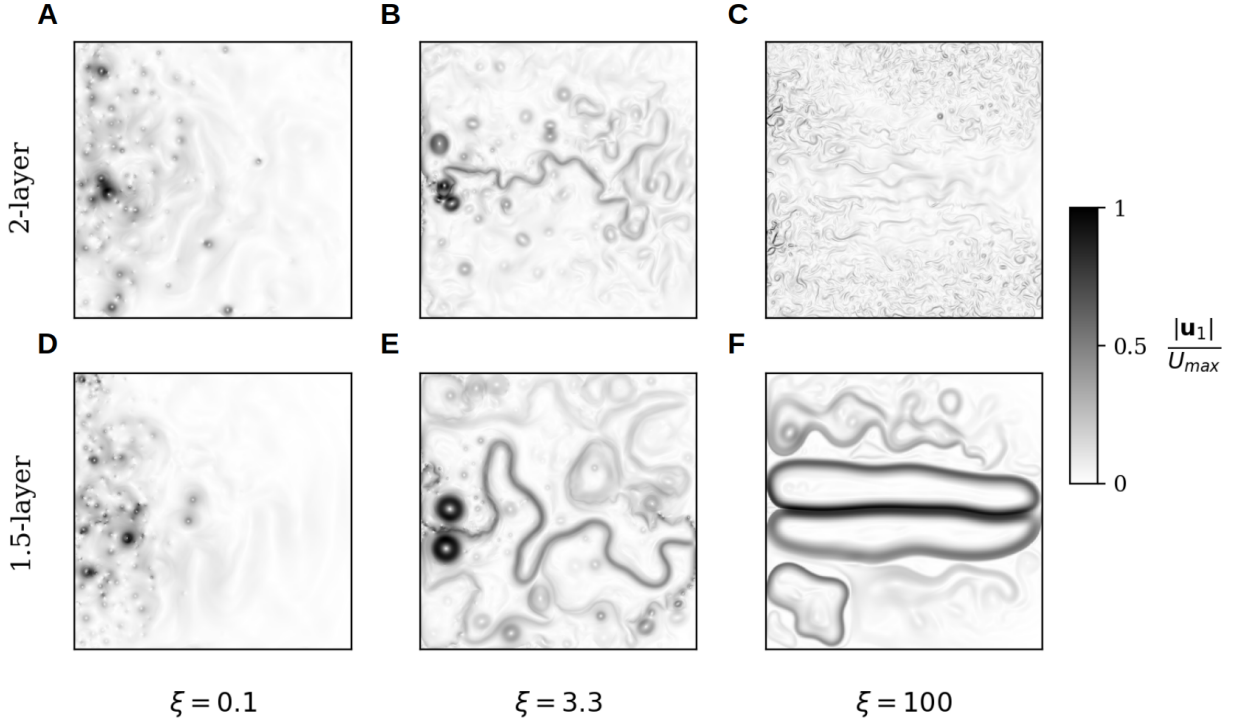


FIG. 7. Comparison of instantaneous surface velocity snapshots between the 2-layer model at $\delta = 0.01$ (top row) and the 1.5-layer model (bottom row), at (A,D) $\xi = 0.1$, (B,E) $\xi = 3.3$ and (C,F) $\xi = 100$. The maximum velocities in the instantaneous flow fields (renormalized by U_{SV}) for the 2-layer model are 372, 166 and 50, for the 1.5-layer model they are 361, 208 and 105. The simulation at $\xi = 100$ in the 1.5-layer model is still in the process of spin-up.

surface intensified configurations.

In conclusion, the emergence of a strong eastward jet detaching from the western boundary is driven by the dynamics of the 1.5-layer model, while the two-layer dynamics are essential for preventing the formation of

intense recirculation and westward jets. This is the central

result of this paper.

6. The Zonostrophic Regime ($10 \lesssim \xi$): Freely Decaying Turbulence on Eastward Flow

If ξ is increased further in the intermediate regime, a loss of western intensification occurs and the system enters a zonostrophic regime (figure 8). Multiple zonal jets populate regions of eastward flow, and a soup of baroclinic eddies forms in regions of westward flow and close to the western boundary. This regime is likely the same as reported on in Nadiga and Straub (2019). In this section, we show that it is best understood as the consequence of strong zonal asymmetry of baroclinic instability.

Following the idea that westward flow produces eddies at scales close to L_d it is possible to obtain a scaling for the turbulent velocity scale. If the flow is mostly constrained to the upper layer, we obtain a scaling relation by balancing the energy injection through a Sverdrup interior with dissipation close to a scale L_d . Omitting interactions with the lower layer, the upper layer energy balance reads

$$\int \frac{\tau \cdot \mathbf{u}_1}{H_1} dA = \nu \int (\nabla^2 \psi)^2 dA, \quad (11)$$

which scales as

$$\frac{\tau_0 U_{Sv} L^2}{H_1} \sim \frac{\nu U_{eddy}^2 L^2}{L_d^2} \quad (12)$$

and leads to

$$\frac{U_{eddy}}{U_{Sv}} = \frac{C}{\sqrt{\nu} \xi}, \quad (13)$$

where C is a constant. Figure 3B shows this relation with $C = 0.05$. U_{eddy} is thought to describe the eddies observed in the regions of mean westward flow in the zonostrophic regime, and fits well with the total average speed (figure 3B).

In region of eastward flow, multiple zonal jets form (figure 4, 8A). In the absence of western intensification these jets can no longer be considered as direct extensions of an overshooting western boundary current as in the previous section, neither can they be the product of a purely local inverse cascade as in Berloff et al. (2009b,a) because of the stability of the background Sverdrup flow. Here we show that these jets are the result of turbulence, generated through baroclinic instability in the westward flowing regions, which freely decays in a region of stable eastward flow.

Turbulence on a β -plane has a tendency to form zonal jets by creating locally homogenized regions of potential vorticity commonly referred to as staircases (Dritschel and McIntyre 2008) with a spacing of $L^{Rh} = 2\pi\sqrt{U_{turb}/\beta}$ (Rhines 1975), where U_{turb} is a turbulent velocity scale of the flow. Here, in a 2-layer model with the deeper layer at

rest, the surface layer dynamics around an eastward mean flow U_m see an effective beta-effect $\beta + U_m/L_d^2$ (Burgess and Dritschel 2022). The jet spacing then scales like

$$L_{eff}^{Rh} = 2\pi \sqrt{\frac{U_{turb}}{\beta + \frac{U_m}{L_d^2}}}. \quad (14)$$

This formula holds under the assumption of an upper layer surface-intensified eastward flow, which breaks down when this mean flow is baroclinically unstable. Considering stretching by Sverdrup flow, this occurs in gyres at $\xi = 1/\delta$. Therefore, when δ is asymptotically small, there remains a range of criticality parameters $\xi \gg 1$ such that (14) is valid, with an effective beta term that is dominated by the stretching term induced by eastward Sverdrup flow ($U_m/L_d^2 \gg \beta$).

We argue that this stretching is responsible for the apparition of multiple eastward jets and the creation of potential vorticity staircases in our simulations at $\xi = 10, 33$ and 100. The scaling in equation (14) is confirmed in figure 8C. Following the idea of non-local generation of turbulence, U_{turb} was calculated close to the western boundary and the jet scale and U_m in the bulk (figure 8A, "turbulence" and "staircases" respectively). To further support the enhanced stretching on an imposed background flow, the scarce data available from the basin-scale runs was complemented with periodic simulations of decaying surface-intensified turbulence with an imposed background flow. Although slightly offset, they also follow the jet spacing given by equation (14). For further details on the periodic runs, extraction of U_{turb} , U_m and the jet scale the reader may consult Appendix D.

Replacing the scaling for U_{turb} by U_{eddy} and U_m by U_{Sv} in equation (14), it is possible to predict the onset of the zonostrophic regime by equating L_{eff}^{Rh} and the size of the region of eastward flow, $L/2$. Although the result depends on a number of constants in front of the scaling relations, simply inserting U_{eddy} as shown in figure 3B into equation (14) yields a predicted regime change at $\xi \approx 9$, consistent with numerical experiments. At higher criticality, a precise prediction of the jet scale fails, arguably due to the difference between local and global values of root-mean-square velocity and an incorrect stretching due to the departure from Sverdrup flow at large scales.

In summary, the zonostrophic regime is a result of the strong asymmetry of baroclinic instability in the limit of small δ . Sverdrup theory and classic descriptions of western boundary currents no longer match the observed flow, even on a qualitative level. Instead, a clear separation of scales between mean flow heterogeneity and the size of the turbulent structures appears, and the regime is well

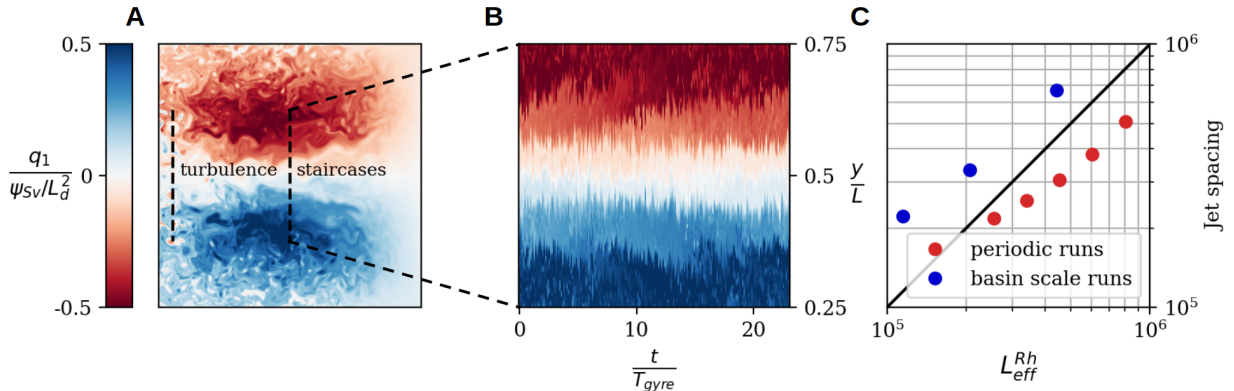


Fig. 8. (A) Snapshot of potential vorticity staircases at $\delta = 0.01$, $\xi = 33$ with (B) Hovmöller diagram taken at $x/L = 1/2$ and $1/4 < y/L < 3/4$. Time is non-dimensionalised by the gyre turnover time $T_{Gyre} = L/U_{Sv}$. (C) Comparison of jet scaling with effective Rhines scale L_{eff}^{Rh} . The basin scale runs plotted on this curve are those at $\xi = 10, 32$ and 100 .

understood in the framework of unbounded turbulence on an effective β -plane.

7. Discussion and Conclusion

We found that stratification properties play a crucial role in the emergence of surface-intensified eastward jets in two-layer quasi-geostrophic models without bottom friction. The important nondimensional numbers in this context are the criticality parameter ξ , which decreases with the density difference between layers, and δ , the ratio of the depths of the two layers.

When the criticality parameter is smaller than one, turbulence takes the form of a western-intensified vortex gas. An energetic eastward jet at the inter-gyre boundary only emerges when ξ is roughly between 1 and 10. As the criticality parameter increases further the flow enters a zonostrophic regime, with multiple jets filling the eastward part of the gyres and baroclinic eddies occupying the westward part. Eventually, when $\xi > 1/\delta$, the flow starts to become barotropic.

The emergence of the eastward jet detaching from the western boundary when $\xi > 1$ can be understood from two perspectives. First, linear stability analysis indicates that the jet's formation coincides with the stabilization of the inertial western boundary layer, suggesting an interpretation of the westward jet as an overshooting boundary layer. Second, the observed transition from a vortex gas to eastward jets also occurs in unbounded 1.5-layer dynamics when the energy injection length scale exceeds the Rossby radius of deformation L_d . Here, we argue that both mechanisms, albeit of different nature, are active in the two-layer model of wind-driven circulation when $\xi \sim 1$.

In the 1.5-layer model, the eastward jet emerges similarly to the two-layer case when ξ increases above one. However, this process also leads to westward jets, which are not present in the two-layer model. We showed that these westward jets are disintegrated by baroclinic instability, while eastward jets remain baroclinically stable, explaining the establishment of the western boundary current extension as a single eastward jet.

In this study we investigated values of δ smaller than the usual oceanic configuration, but the flow dynamics at small δ remain relevant for understanding the classical configuration. Despite the asymptotically small value of δ , the flow of the reference case shares many properties with the flow obtained with $\delta \sim 0.2$, free-slip boundary conditions and bottom friction (Holland 1978) (see also appendix A). The underlying dynamical similarity between the classical flow configuration and the regime at $\delta = 0.01$ becomes apparent in the results of linear stability analysis. Both configurations feature unstable westward Sverdrup flow, but eastward Sverdrup flow and inertial boundary currents are stable.

A common concern with quasi-geostrophic models of ocean gyres is how sensitive they are to boundary conditions. While free-slip boundary conditions tend to produce more intense eastward jets (Haidvogel et al. 1992; Dremble et al. 2011; Nasser et al. 2023), we showed that jets still form in a no-slip configuration if the stratification is appropriately chosen. One reason for this insensitivity to boundary conditions observed here might be the stability of the inertial western boundary layer in the two-layer system (Fig. 5), which is easier to model with free-slip boundary conditions (Ierley and Young 1991).

The main result of this article is that in a baroclinic model the gyre pattern and the eastward jet are primarily shaped by stratification. This contrasts with the strong dependence of the structure of turbulent barotropic gyres on dissipative processes (Fox-Kemper and Pedlosky 2004). To support the lesser role of dissipation in baroclinic configurations, we note the striking similarity between the free-slip, bottom friction run (figure A1) and the no-slip, no bottom friction run (figure 1), and emphasize that bottom friction is not required to rationalize the emergence of the jet. However, an efficient dissipation mechanism is required to prevent the formation of an energetic vortex gas that may disrupt jet formation (appendix A). Of course, these energetic flows violate quasi-geostrophic assumptions (Scott and Straub 1998) and are prone to ageostrophic energy sinks (Dewar and Hogg 2010; Nikurashin et al. 2013; Brüggemann and Eden 2015), which, besides bottom friction, will likely become important for dissipating eddies in more realistic scenarios.

We conclude that the minimal ingredients for the emergence of a coherent eastward jet extending from western boundary layers in turbulent quasi-geostrophic gyres are: (i) a criticality parameter ξ that is sufficiently large to permit baroclinic instability but sufficiently small to leave surface-intensified Sverdrup flow intact, (ii) a layer depth aspect ratio δ sufficiently small for baroclinic instability to permit eastward jets, but release energy towards eddies in adjacent areas of westward recirculation, and (iii) an efficient energy sink which suppresses unrealistic eddy-driven flows.

Acknowledgments. This project has received financial support from the CNRS through the 80 Prime program, and was performed using HPC resources at PSMN Lyon and GENCI HPC (allocation A0150112020).

Data availability statement. Data used in this article were produced with the code qgw (<https://doi.org/10.5281/zenodo.13990523>). Python notebooks for calculation of potential vorticity homogenization and linear stability analysis are available online (<https://doi.org/10.5281/zenodo.14055345>). Please contact the corresponding author for access to simulation data.

APPENDIX A

Comparison to Realistic Values of δ

A more traditional approach to modelling energy dissipation in quasi-geostrophic wind-driven gyres is to apply free-slip boundary conditions and model bottom friction via the inclusion of a linear drag term of the form $-r\nabla^2\psi_2$ on the right hand side of the equation for the bottom layer in equation (4) (Holland 1978). A standard run, at $\delta = 1/6$, is shown in figure A1, sharing many of the properties listed for the reference run: western and surface intensification, homogenization of potential vorticity inside the gyres and the presence of a strong eastward jet at the interface between the homogenized potential vorticity pools.

If bottom friction is replaced by a no-slip boundary condition as an energy sink, an energetic vortex gas was observed instead of the jet at $\xi = 1$, $\delta = 1/6$ (figure A2). Jet solutions emerged under three conditions: (i) with the addition of bottom friction, (ii) with an increase in viscosity, or (iii) with a decrease in the layer depth aspect ratio. Its reappearance at lower $\delta = 0.01$, presented as the reference run in the main text, may be understood as the consequence of the stability island of the western boundary layer becoming larger as δ is decreased (figure 5). An inertial overshoot of the western boundary layer remains possible at smaller values of L_d , where smaller vortices dissipate energy more effectively (equation (13)). These vortices thus become less energetic, and the jet may support their presence.

APPENDIX B

Details on the Regime of Weak Stratification

Potential Vorticity Homogenization Theory

Calculations on potential vorticity homogenization in 2-layer oceanic gyres can be found in classical textbooks (Vallis 2017). A simple extension including unequal layer

depths is given here, with a focus on the mechanism responsible for the onset of homogenization in the lower layer. We write the quasi-geostrophic equations on a modal basis, neglecting time derivatives and relative vorticity contributions, but including diffusion of potential vorticity instead of relative vorticity.

$$\beta \frac{\partial \psi_{bt}}{\partial x} = \frac{\nabla \times \tau}{H_1 + H_2} \quad (\text{B1})$$

$$\beta \frac{\partial \psi_{bc}}{\partial x} - \frac{1}{L_d^2} J(\psi_{bt}, \psi_{bc}) = \frac{\nabla \times \tau}{H_1} + \nu \frac{\nabla^2 \psi_{bc}}{L_d^2} \quad (\text{B2})$$

$$\psi_{bt} = \frac{H_1 \psi_1 + H_2 \psi_2}{H_1 + H_2} \quad (\text{B3})$$

$$\psi_{bc} = \psi_1 - \psi_2 \quad (\text{B4})$$

When L_d is large, the advective term for the baroclinic mode can be neglected and all transport happens in the upper layer. A change in regime occurs when the advective term of the baroclinic mode starts to be of the same order of magnitude as the β -term. Using Sverdrup scalings for $\psi_{bc/bt}$ as obtained from equation (B3,B4), this occurs when

$$1 \sim \frac{\frac{1}{L_d^2} J(\psi_{bt}, \psi_{bc})}{\beta \frac{\partial \psi_{bc}}{\partial x}} \sim \frac{U_{Sv} H_1}{\beta L_d^2 (H_1 + H_2)} \sim \delta \xi. \quad (\text{B5})$$

Baroclinic instability is not required for this change to occur, it is only the baroclinic/barotropic advection that alters the dynamical balance of the Sverdrup flow. However, baroclinic instability will always be present at the onset of inertial recirculation in surface-intensified flows, its sole effect being represented by the presence of weak diffusion of potential vorticity. This diffusion sets the final flow by homogenizing potential vorticity in the lower layer. The solution is then given by matching the contours at the center latitude $y = L/2$ and separating regions of blocked and closed geostrophic contours. The solution is written in terms of

$$\bar{\psi} = \frac{2\pi\tau_0}{\beta(H_1 + H_2)} \sin\left(\frac{2\pi y}{L}\right) \left(1 - \frac{x}{L}\right) \quad (\text{B6})$$

$$\bar{q} = \beta y + \frac{\bar{\psi}}{L_d^2} \quad (\text{B7})$$

Geostrophic contours are blocked in the northern gyre if $\bar{q} > \beta L/2$ and in the southern gyre if $\bar{q} < \beta L/2$. The upper layer solution is then given by

$$\psi_1 = \frac{(H_1 + H_2)\bar{\psi}}{H_1}. \quad (\text{B8})$$

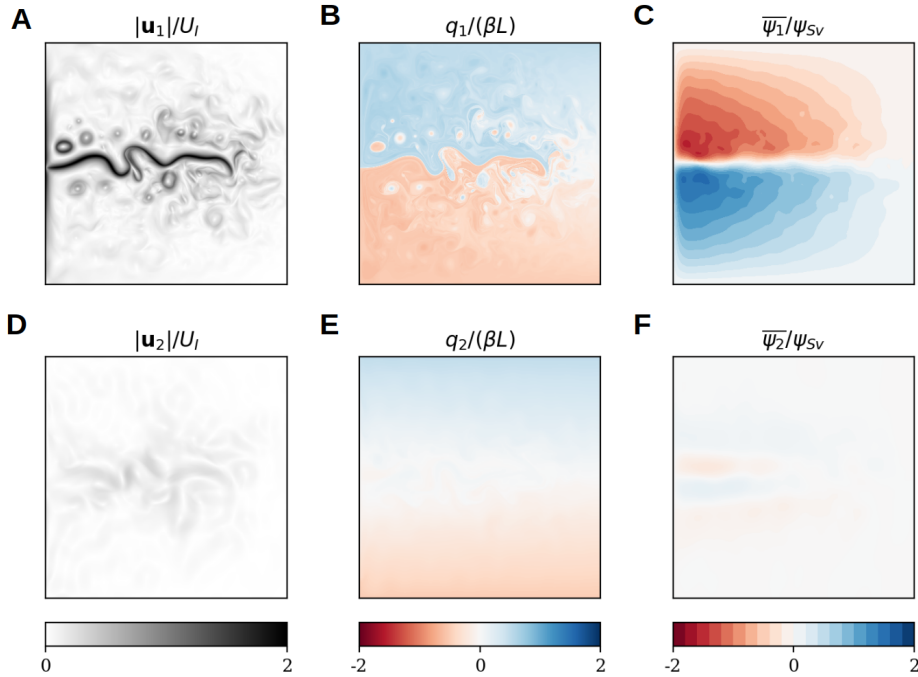


FIG. A1. (A, D) Flow speed, (B, E) potential vorticity and (C, F) mean stream function of a simulations at $\delta = 1/6$ ($H_1 = 666$ m, $H_2 = 3334$), $\xi = 1.3$, with free-slip boundary condition and a drag coefficient $r = 3.3 \times 10^{-7} \text{ s}^{-1}$. Note the similarity between this regime and the reference run presented in figure 1.

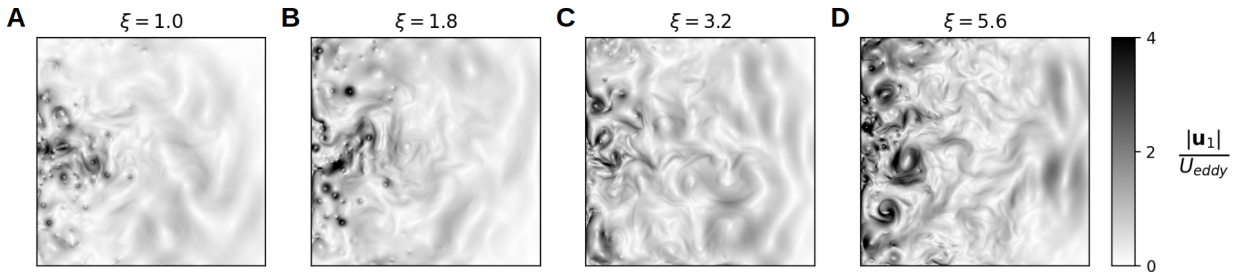


FIG. A2. Upper layer flow speed of runs without bottom friction at $\delta = 1/6$ ($H_1 = 666$ m, $H_2 = 3334$ m) for (A) $\xi = 1$, (B) $\xi = 1.8$, (C) $\xi = 3.2$ and (D) $\xi = 5.6$. Note the absence of jets.

Else, for a closed contour, homogenization of potential vorticity in the lower layer leads to availability statement.

$$\psi_1 = \bar{\psi} - \frac{H_1}{H_2} \beta L_d^2 \left(y - \frac{L}{2} \right). \quad (\text{B9})$$

The lower layer $\psi_2 = \left((H_1 + H_2) \bar{\psi} - H_1 \psi_1 \right) / H_2$ carries the remaining transport to satisfy the barotropic Sverdrup balance. The lines in figure 3A are computed numerically from this solution. Details on this numerical calculation may be found in the code repository linked in the Data

a. Observed Flows at $\delta = 0.01$

At equal layer depths a complete barotropization occurs when $\delta \xi > 1$ (figure 3). When δ is small, however, both the mean flow and the turbulent flow features retain a strong baroclinic signature (figure B1). In the lower layer a Sverdrup Flow starts to grow and potential vorticity homogenizes. The upper layer appears to stay in the zonostrophic regime, with strong zonal asymmetry of the

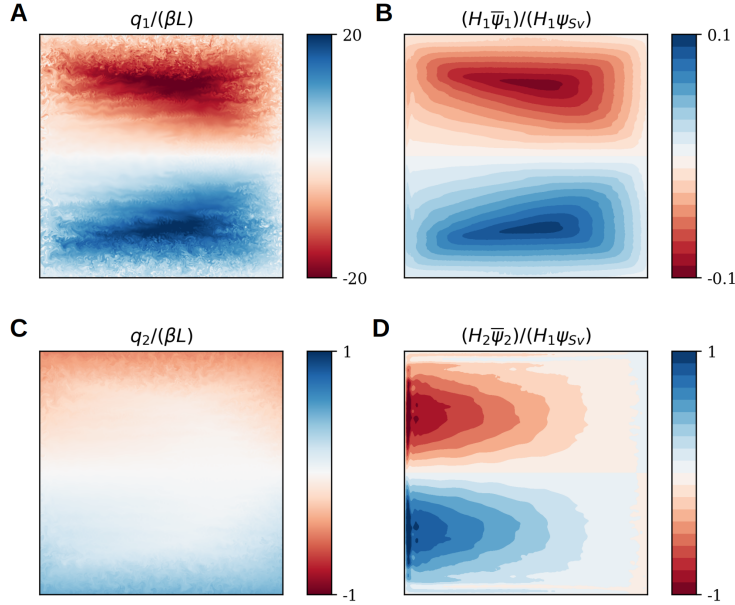


FIG. B1. (A,C) Potential vorticity snapshots and (B,D) mean transport of the weak stratification regime low aspect ratio ($\xi = 10^3$, $\delta = 0.01$). Baroclinic activity remains strong even though a Sverdrup flow starts to grow in the lower layer.

turbulent flow features and a complete loss of western intensification. We discuss here the asymptotic nature of this flow as $\xi \rightarrow \infty$. From equation B9 it can be shown that even in the homogenized region the baroclinic zonal shear leads to a criticality of

$$\frac{u_{bc}}{\beta L_d^2} = \frac{1}{\delta}, \quad (\text{B10})$$

rationalising the strong activity of baroclinic instability in the weakly stratified regime when δ is small. Nonetheless, a complete barotropization is expected at larger ξ than those explored here (figure 3A), although viscosity might prevent barotropization of turbulence by direct dissipation in the upper layer (equation 13). Remarkably, potential vorticity homogenization theory works indifferent to the complex dynamics in the upper layer.

APPENDIX C

Instability Calculations

Linearising the QG equations around a base state with upper layer velocity only, we obtain:

$$\frac{\partial q_1}{\partial t} + J(\psi_1, Q_1) + J(\Psi_1, q_1) = \nu \nabla^4 \psi_1 \quad (\text{C1})$$

$$\frac{\partial q_2}{\partial t} + J(\psi_2, Q_2) = \nu \nabla^4 \psi_2 \quad (\text{C2})$$

Here $q_{1/2}, \psi_{1/2}$ denote the perturbation fields but are defined as in the main text. The base state is given by

$$Q_1 = \nabla^2 \Psi_1 - \frac{1-\delta}{L_d^2} \Psi_1 + \beta y, \quad Q_2 = \frac{\delta}{L_d^2} \Psi_1 + \beta y. \quad (\text{C3})$$

For the linear stability analysis, three base states were defined. For the interior flow, the base state was given by $\Psi_1 = \pm U_{Sv} y$, where the \pm stands for eastward or westward flow respectively. In these calculations, ν was set to zero. The problem is governed by two non-dimensional numbers, ξ and δ .

The instability analysis of the western boundary layer was carried out by assuming that the problem is invariant in the y -direction. The base profile is defined as in equation 10 and meant to resemble a double-deck boundary layer structure with an inertial thickness of δ_I and a viscous sublayer δ_P . As in the simulations, the sublayer thickness was set to $\delta_P \approx 3$ km and the inertial layer thickness to $\delta_I \approx 72$ km. The explicit dependence on δ_I and δ_P is not explored further.

The instability problem for interior flow is decomposed on Fourier modes and analytically solvable, but the expressions are cumbersome and not very insightful. They can also be found in Pedlosky (1987) and will therefore not be reproduced explicitly, and the reader is referred to figures 5 for results. For the western boundary current, decomposition in y is carried out on a Fourier basis, too, and the eigenvectors in x are solved for numerically using 4th order finite-element discretisation of the derivatives. Details on this calculation may be found in the code repository linked in the Data availability statement. Again, the results are shown in the main text.

APPENDIX D

Details on the Zonostrophic Regime

In order to compare jet spacing in the zonostrophic regime with L_{eff}^{Rh} , we measured U_{turb} as the average fluctuation speed along the meridional line $L/4 < y < 3L/4$, $x = 3\delta_I$ and U_m was measured as the mean transport across the line $L/4 < y < 3L/4$, $x = L/2$ divided by $L/2$ (figure 8A, lines entitled "turbulence" and "staircases" respectively). In order to determine the number of jets, we calculate the histogram of the potential vorticity along the Hovmöller diagram at mid-basin (figure 8B). Finally, to obtain the jet spacing, the meridional size over which the histogram was obtained is then divided by the number of distinct peaks that exceed the standard deviation of the histogram, corresponding to the number of distinct homogenized regions.

We performed additional runs with periodic boundary conditions to complement the basin-scale runs. An example simulation can be seen in figure D1, where the velocity perturbation is denoted as \mathbf{u}' . The initial flow fields are given by

$$\psi_1(t=0) = \psi'_1 - U_m y \quad (D1)$$

$$\psi_2(t=0) = 0 \quad (D2)$$

$$q_1(t=0) = q'_1 + \frac{1-\delta}{L_d^2} U_m y \quad (D3)$$

$$q_2(t=0) = -\frac{\delta}{L_d^2} U_m y \quad (D4)$$

with $q'_1 = \nabla^2 \psi'_1 - (1-\delta)/L_d^2 (\psi'_2 - \psi'_1) + \beta y$. The stream function was initialised with a randomly generated signal centered around the wavenumber $1/L_d$, meaning to represent turbulence generated close to the western boundary due to baroclinic instability, and then left to freely decay. In all these simulations the deformation radius was fixed at $L_d = 40.7$ km, $U_m = 0.2$ m/s, $\delta = 0.01$

and the domain size was set to $L = 1523$ km. It was also necessary to decrease viscosity to $\nu = 0.1$ m²/s in order to obtain final states with clear staircases. This required a numerical resolution of 2048x2048 grid points, and all simulations were run until mixing of potential vorticity transferred the complete perturbation energy into zonal jets. All other parameters are the same as in the surface-intensified basin-scale simulations (table 1).

To show the dependence of the jet spacing on the initial perturbation, we carried out five periodic simulations varying the turbulent velocity scale U_{turb} . It is defined here as

$$U_{turb} = \sqrt{\frac{1}{L^2} \int |\nabla \psi'_1|^2 dA} \quad (D5)$$

at the time of initiation, and was varied between $\beta L_d^2 + U_m$ and $10(\beta L_d^2 + U_m)$. To determine the jet spacing the histogram of potential vorticity is taken of a snapshot of the final state over the entire domain, and then the same procedure as for the basin-scale simulations is followed to extract the jet scale.

Figure 8B also shows the slow polewards displacement of the staircases of potential vorticity in the basin-scale runs. Nadiga and Straub (2019) suggested that the displacement speed is correlated with U_{Sv} , however in our simulations it seemed to match better with the maximum Rossby wave speed, βL_d^2 .

References

- Ajayi, A., J. Le Sommer, E. Chassignet, J.-M. Molines, X. Xu, A. Albert, and E. Cosme, 2020: Spatial and temporal variability of the north atlantic eddy field from two kilometric-resolution ocean models. *J. Geophys. Res.*, **125** (5), e2019JC015 827, <https://doi.org/10.1029/2019JC015827>.
- Arbic, B. K., and G. R. Flierl, 2003: Coherent vortices and kinetic energy ribbons in asymptotic, quasi two-dimensional f-plane turbulence. *Physics of fluids*, **15** (8), 2177–2189, <https://doi.org/10.1063/1.1582183>.
- Arbic, B. K., and G. R. Flierl, 2004a: Baroclinically unstable geostrophic turbulence in the limits of strong and weak bottom ekman friction: Application to midocean eddies. *Journal of Physical Oceanography*, **34** (10), 2257–2273, [https://doi.org/10.1175/1520-0485\(2004\)034<2257:BUGTIT>2.0.CO;2](https://doi.org/10.1175/1520-0485(2004)034<2257:BUGTIT>2.0.CO;2).
- Arbic, B. K., and G. R. Flierl, 2004b: Effects of mean flow direction on energy, isotropy, and coherence of baroclinically unstable beta-plane geostrophic turbulence. *Journal of physical oceanography*, **34** (1), 77–93, [https://doi.org/10.1175/1520-0485\(2004\)034<0077:EOMFDO>2.0.CO;2](https://doi.org/10.1175/1520-0485(2004)034<0077:EOMFDO>2.0.CO;2).
- Berloff, P., I. Kamenkovich, and J. Pedlosky, 2009a: A mechanism of formation of multiple zonal jets in the oceans. *Journal of Fluid Mechanics*, **628**, 395–425, <https://doi.org/10.1017/S0022112009006375>.

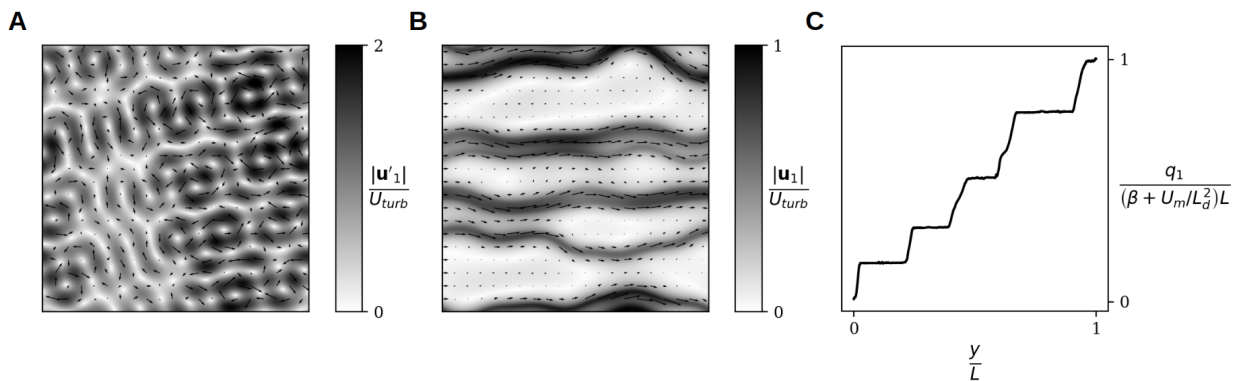


FIG. D1. (A) Initial velocity perturbation, (B) final velocity fields and (C) meridional profile of potential vorticity for the periodic staircase run at injection velocity $U_{turb} = 3.2(\beta L_d^2 + U_m)$.

- Berloff, P., I. Kamenkovich, and J. Pedlosky, 2009b: A Model of Multiple Zonal Jets in the Oceans: Dynamical and Kinematical Analysis. *Journal of Physical Oceanography*, **39** (11), 2711–2734, <https://doi.org/10.1175/2009JPO4093.1>.
- Berloff, P. S., and J. C. McWilliams, 1999a: Large-Scale, Low-Frequency Variability in Wind-Driven Ocean Gyres. *Journal of Physical Oceanography*, **29** (8), 1925–1949, [https://doi.org/10.1175/1520-0485\(1999\)029<1925:LSELFVI>2.0.CO;2](https://doi.org/10.1175/1520-0485(1999)029<1925:LSELFVI>2.0.CO;2).
- Berloff, P. S., and J. C. McWilliams, 1999b: Quasigeostrophic Dynamics of the Western Boundary Current. *Journal of Physical Oceanography*, **29** (10), 2607–2634, [https://doi.org/10.1175/1520-0485\(1999\)029<2607:QDOTWB>2.0.CO;2](https://doi.org/10.1175/1520-0485(1999)029<2607:QDOTWB>2.0.CO;2).
- Bouchet, F., and A. Venaille, 2012: Statistical mechanics of two-dimensional and geophysical flows. *Physics reports*, **515** (5), 227–295, <https://doi.org/10.1016/j.physrep.2012.02.001>.
- Bretherton, F. P., and D. B. Haidvogel, 1976: Two-dimensional turbulence above topography. *Journal of Fluid Mechanics*, **78** (1), 129–154, <https://doi.org/10.1017/S002211207600236X>.
- Brüggemann, N., and C. Eden, 2015: Routes to dissipation under different dynamical conditions. *Journal of Physical Oceanography*, **45** (8), 2149–2168, <https://doi.org/10.1175/JPO-D-14-0205.1>.
- Burgess, B., and D. G. Dritschel, 2022: Potential vorticity fronts and the late-time evolution of large-scale quasi-geostrophic flows. *Journal of Fluid Mechanics*, **939**, A40, <https://doi.org/10.1017/jfm.2022.194>.
- Cessi, P., G. Ierley, and W. Young, 1987: A Model of the Inertial Recirculation Driven by Potential Vorticity Anomalies. *Journal of Physical Oceanography*, **17** (10), 1640–1652, [https://doi.org/10.1175/1520-0485\(1987\)017<1640:AMOTIR>2.0.CO;2](https://doi.org/10.1175/1520-0485(1987)017<1640:AMOTIR>2.0.CO;2).
- Cessi, P., and G. R. Ierley, 1995: Symmetry-Breaking Multiple Equilibria in Quasigeostrophic, Wind-Driven Flows. [https://doi.org/10.1175/1520-0485\(1995\)025<1196:SBMEIQ>2.0.CO;2](https://doi.org/10.1175/1520-0485(1995)025<1196:SBMEIQ>2.0.CO;2).
- Charney, J. G., 1955: The gulf stream as an inertial boundary layer. *Proceedings of the National Academy of Sciences*, **41** (10), 731–740, <https://doi.org/10.1073/pnas.41.10.731>.
- Chassignet, E. P., and D. P. Marshall, 2008: Gulf stream separation in numerical ocean models. *Ocean Modeling in an Eddy Regime*, M. Hecht, and H. Hasumi, Eds., Vol. 177, Amer. Geophys. Union, 39–61, <https://doi.org/10.1029/177GM05>.
- Chassignet, E. P., and X. Xu, 2021: On the importance of high-resolution in large-scale ocean models. *Adv. Atmos. Sci.*, 1–14, <https://doi.org/10.1007/s00376-021-0385-7>.
- Dereemble, B., A. M. Hogg, P. Berloff, and W. K. Dewar, 2011: On the application of no-slip lateral boundary conditions to coarsely resolved ocean models. *Ocean Modelling*, **39** (3-4), 411–415, <https://doi.org/10.1016/j.ocemod.2011.05.002>.
- Dereemble, B., E. R. Johnson, and W. K. Dewar, 2017: A coupled model of interior balanced and boundary flow. *Ocean Model.*, **119**, 1–12, <https://doi.org/10.1016/j.ocemod.2017.09.003>.
- Dewar, W. K., and A. M. Hogg, 2010: Topographic inviscid dissipation of balanced flow. *Ocean Modelling*, **32** (1-2), 1–13, <https://doi.org/10.1016/j.ocemod.2009.03.007>.
- Dijkstra, H. A., and M. Ghil, 2005: Low-frequency variability of the large-scale ocean circulation: A dynamical systems approach. *Reviews of Geophysics*, **43** (3), <https://doi.org/10.1029/2002RG000122>.
- Dritschel, D., and M. McIntyre, 2008: Multiple jets as pv staircases: The phillips effect and the resilience of eddy-transport barriers. *Journal of the Atmospheric Sciences*, **65** (3), 855–874, <https://doi.org/10.1175/2007JAS2227.1>.
- Forget, G., J.-M. Campin, P. Heimbach, C. N. Hill, R. M. Ponte, and C. Wunsch, 2015: Ecco version 4: an integrated framework for non-linear inverse modeling and global ocean state estimation. *Geosci. Model Dev.*, **8** (10), 3071–3104, <https://doi.org/10.5194/gmd-8-3071-2015>.
- Fox-Kemper, B., 2004: Wind-driven barotropic gyre ii: Effects of eddies and low interior viscosity. *Journal of Marine Research*, **62** (2), 195–232.
- Fox-Kemper, B., and J. Pedlosky, 2004: Wind-driven barotropic gyre i: Circulation control by eddy vorticity fluxes to an enhanced removal region. *Journal of Marine Research*, **62** (2), 169–193.
- Frishman, A., J. Laurie, and G. Falkovich, 2017: Jets or vortices—what flows are generated by an inverse turbulent cascade? *Physical Review Fluids*, **2** (3), 032602, <https://doi.org/10.1103/PhysRevFluids.2.032602>.
- Gallet, B., and R. Ferrari, 2020: The vortex gas scaling regime of baroclinic turbulence. *Proceedings of the National Academy of Sciences*, **117** (9), 4491–4497, <https://doi.org/10.1073/pnas.1916272117>.

- Grooms, I., L.-P. Nadeau, and K. S. Smith, 2013: Mesoscale eddy energy locality in an idealized ocean model. *Journal of physical oceanography*, **43** (9), 1911–1923, <https://doi.org/10.1175/JPO-D-13-036.1>.
- Hadjerci, G., and B. Gallet, 2023: Vortex core radius in baroclinic turbulence: Implications for scaling predictions. *Physical Review Fluids*, **8** (9), 094 501, <https://doi.org/10.1103/PhysRevFluids.8.094501>.
- Hadjerci, G., and B. Gallet, 2024: Two-layer baroclinic turbulence with arbitrary layer depths. *Physical Review Fluids*, **9** (5), L051 802, <https://doi.org/10.1103/PhysRevFluids.9.L051802>.
- Haidvogel, D. B., J. C. McWilliams, and P. R. Gent, 1992: Boundary Current Separation in a Quasigeostrophic, Eddy-resolving Ocean Circulation Model. *Journal of Physical Oceanography*, **22** (8), 882–902, [https://doi.org/10.1175/1520-0485\(1992\)022\(0882:BCSIAQ\)2.0.CO;2](https://doi.org/10.1175/1520-0485(1992)022(0882:BCSIAQ)2.0.CO;2).
- Held, I. M., and V. D. Larichev, 1996: A scaling theory for horizontally homogeneous, baroclinically unstable flow on a beta plane. *J. Atmos. Sci.*, **53** (7), 946–952, [https://doi.org/10.1175/1520-0469\(1996\)053\(0946:ASTFHH\)2.0.CO;2](https://doi.org/10.1175/1520-0469(1996)053(0946:ASTFHH)2.0.CO;2).
- Holland, W. R., 1978: The role of mesoscale eddies in the general circulation of the ocean—numerical experiments using a wind-driven quasi-geostrophic model. *Journal of Physical Oceanography*, **8** (3), 363–392, [https://doi.org/10.1175/1520-0485\(1978\)008\(0363:TROMEI\)2.0.CO;2](https://doi.org/10.1175/1520-0485(1978)008(0363:TROMEI)2.0.CO;2).
- Holland, W. R., and W. J. Schmitz, 1985: Zonal penetration scale of model midlatitude jets. *Journal of physical oceanography*, **15** (12), 1859–1875, [https://doi.org/10.1175/1520-0485\(1985\)015\(1859:ZPSOMM\)2.0.CO;2](https://doi.org/10.1175/1520-0485(1985)015(1859:ZPSOMM)2.0.CO;2).
- Ierley, G., and W. Young, 1988: Inertial recirculation in a β -plane corner. *Journal of physical oceanography*, **18** (4), 683–689, [https://doi.org/10.1175/1520-0485\(1988\)018\(0683:IRIAPC\)2.0.CO;2](https://doi.org/10.1175/1520-0485(1988)018(0683:IRIAPC)2.0.CO;2).
- Ierley, G., and W. Young, 1991: Viscous instabilities in the western boundary layer. *Journal of physical oceanography*, **21** (9), 1323–1332, [https://doi.org/10.1175/1520-0485\(1991\)021\(1323:VIITWB\)2.0.CO;2](https://doi.org/10.1175/1520-0485(1991)021(1323:VIITWB)2.0.CO;2).
- Ierley, G. R., 1990: Boundary layers in the general ocean circulation. *Annual review of fluid mechanics*, **22** (1), 111–140, <https://doi.org/10.1146/annurev.fl.22.010190.000551>.
- Ierley, G. R., and O. G. Ruehr, 1986: Analytic and Numerical Solutions of a Nonlinear Boundary-Layer Problem. *Studies in Applied Mathematics*, **75** (1), 1–36, <https://doi.org/10.1002/sapm19867511>.
- Jansen, M., and R. Ferrari, 2012: Macroturbulent equilibration in a thermally forced primitive equation system. *J. Atmos. Sci.*, **69** (2), 695–713, <https://doi.org/10.1175/JAS-D-11-041.1>.
- Kubokawa, A., 2023: Meridional Location and Profile of a Prematurely Separated WBC Extension Jet in a Two-Layer System. *Journal of Physical Oceanography*, **53** (4), 995–1010, <https://doi.org/10.1175/JPO-D-21-0313.1>.
- Kukharkin, N., S. A. Orszag, and V. Yakhot, 1995: Quasicrystallization of vortices in drift-wave turbulence. *Physical review letters*, **75** (13), 2486, <https://doi.org/10.1103/PhysRevLett.75.2486>.
- Kurashina, R., P. Berloff, and I. Shevchenko, 2021: Western boundary layer nonlinear control of the oceanic gyres. *Journal of Fluid Mechanics*, **918**, A43, <https://doi.org/10.1017/jfm.2021.384>.
- Marshall, D., and J. Marshall, 1992: Zonal Penetration Scale of Midlatitude Oceanic Jets. *Journal of Physical Oceanography*, **22** (9), 1018–1032, [https://doi.org/10.1175/1520-0485\(1992\)022\(1018:ZPSOMO\)2.0.CO;2](https://doi.org/10.1175/1520-0485(1992)022(1018:ZPSOMO)2.0.CO;2).
- Marshall, J., and G. Nurser, 1986: Steady, free circulation in a stratified quasi-geostrophic ocean. *J. Phys. Oceanogr.*, **16**, 1799–1813, [https://doi.org/10.1175/1520-0485\(1986\)016\(1799:SFCIAS\)2.0.CO;2](https://doi.org/10.1175/1520-0485(1986)016(1799:SFCIAS)2.0.CO;2).
- Miller, L., B. Deremble, and A. Venaille, 2024: Gyre turbulence: Anomalous dissipation in a two-dimensional ocean model. *Physical Review Fluids*, **9** (5), L051 801, <https://doi.org/10.1103/PhysRevFluids.9.L051801>.
- Molemaker, M. J., J. C. McWilliams, and W. K. Dewar, 2015: Submesoscale instability and generation of mesoscale anticyclones near a separation of the California undercurrent. *J. Phys. Oceanogr.*, **45** (3), 613–629, <https://doi.org/10.1175/JPO-D-13-0225.1>.
- Munk, W. H., 1950: On the wind-driven ocean circulation. *Journal of Atmospheric Sciences*, **7** (2), 80–93, [https://doi.org/10.1175/1520-0469\(1950\)007\(0080:OTWDOC\)2.0.CO;2](https://doi.org/10.1175/1520-0469(1950)007(0080:OTWDOC)2.0.CO;2).
- Nadiga, B., and D. Straub, 2010: Alternating zonal jets and energy fluxes in barotropic wind-driven gyres. *Ocean Modelling*, **33** (3-4), 257–269, <https://doi.org/10.1016/j.ocemod.2010.02.007>.
- Nadiga, B. T., and D. N. Straub, 2019: Meridional propagation of zonal jets in ocean gyres. *Zonal Jets: Phenomenology, Genesis, and Physics*, B. Galperin, and P. L. Read, Eds., Cambridge University Press, 284–291.
- Nakano, H., H. Tsujino, and R. Furue, 2008: The Kuroshio Current System as a jet and twin “relative” recirculation gyres embedded in the Sverdrup circulation. *Dynamics of Atmospheres and Oceans*, **45** (3), 135–164, <https://doi.org/10.1016/j.dynatmoce.2007.09.002>.
- Nasser, A.-A., G. Madec, C. de Lavergne, L. Debreu, F. Lemarié, and E. Blayo, 2023: Sliding or stumbling on the staircase: Numerics of ocean circulation along piecewise-constant coastlines. *J. Adv. Model. Earth Syst.*, **15** (5), e2022MS003594, <https://doi.org/10.1029/2022MS003594>.
- Nikurashin, M., G. K. Vallis, and A. Adcroft, 2013: Routes to energy dissipation for geostrophic flows in the southern ocean. *Nature Geoscience*, **6** (1), 48–51, <https://doi.org/10.1038/ngeo1657>.
- Pedlosky, J., 1987: *Geophysical fluid dynamics*. Springer Verlag.
- Rhines, P. B., 1975: Waves and turbulence on a beta-plane. *Journal of Fluid Mechanics*, **69** (3), 417–443, <https://doi.org/10.1017/S0022112075001504>.
- Rhines, P. B., and W. R. Young, 1982: Homogenization of potential vorticity in planetary gyres. *Journal of Fluid Mechanics*, **122**, 347–367, <https://doi.org/10.1017/S0022112082002250>.
- Salmon, R., 1998: *Lectures on geophysical fluid dynamics*. Oxford University Press, USA.
- Salmon, R., G. Holloway, and M. C. Hendershott, 1976: The equilibrium statistical mechanics of simple quasi-geostrophic models. *Journal of Fluid Mechanics*, **75** (4), 691–703, <https://doi.org/10.1017/S0022112076000463>.
- Scott, R., and D. Straub, 1998: Small viscosity behavior of a homogeneous, quasi-geostrophic, ocean circulation model. *Journal of Marine Research*, **56**.

- Sheremet, V., V. Kamenkovich, and A. Pastushkov, 1995: Analysis of the barotropic model of the subtropical gyre in the ocean for finite reynolds numbers. part ii. *Journal of marine research*, **53** (6), 995–1024.
- Simonnet, E., 2005: Quantization of the low-frequency variability of the double-gyre circulation. *Journal of physical oceanography*, **35** (11), 2268–2290, <https://doi.org/10.1175/JPO2806.1>.
- Spall, M., 2000: Generation of strong mesoscale eddies by weak ocean gyres. *Journal of Marine Research*, **58** (1).
- Stommel, H., 1948: The westward intensification of wind-driven ocean currents. *Eos, Transactions American Geophysical Union*, **29** (2), 202–206, <https://doi.org/10.1029/TR029i002p00202>.
- Sun, S., L. Wu, and B. Qiu, 2013: Response of the inertial recirculation to intensified stratification in a two-layer quasigeostrophic ocean circulation model. *Journal of physical oceanography*, **43** (7), 1254–1269, <https://doi.org/10.1175/JPO-D-12-0111.1>.
- Vallis, G. K., 2017: *Atmospheric and oceanic fluid dynamics*. Cambridge University Press.
- Venaille, A., and F. Bouchet, 2011: Oceanic rings and jets as statistical equilibrium states. *Journal of Physical Oceanography*, **41** (10), 1860–1873, <https://doi.org/10.1175/2011JPO4583.1>.
- Venaille, A., T. Dauxois, and S. Ruffo, 2015: Violent relaxation in two-dimensional flows with varying interaction range. *Physical Review E*, **92** (1), 011 001, <https://doi.org/10.1103/PhysRevE.92.011001>.
- Venaille, A., L.-P. Nadeau, and G. Vallis, 2014: Ribbon turbulence. *Physics of Fluids*, **26** (12), 126 605, <https://doi.org/10.1063/1.4904878>.
- Venaille, A., G. K. Vallis, and K. S. Smith, 2011: Baroclinic turbulence in the ocean: Analysis with primitive equation and quasigeostrophic simulations. *Journal of Physical Oceanography*, **41** (9), 1605–1623, <https://doi.org/10.1175/JPO-D-10-05021.1>.
- Veronis, G., 1966: Wind-driven ocean circulation—part 2. numerical solutions of the non-linear problem. *Deep Sea Research and Oceanographic Abstracts*, Vol. 13, 31–55, [https://doi.org/10.1016/0011-7471\(66\)90004-0](https://doi.org/10.1016/0011-7471(66)90004-0).
- Yang, Z., X. Zhai, D. P. Marshall, and G. Wang, 2021: An idealized model study of eddy energetics in the western boundary “graveyard”. *J. Phys. Oceanogr.*, **51** (4), 1265–1282, <https://doi.org/10.1175/JPO-D-19-0301.1>.
- Zhai, X., H. L. Johnson, and D. P. Marshall, 2010: Significant sink of ocean-eddy energy near western boundaries. *Nature Geoscience*, **3** (9), 608–612, <https://doi.org/10.1038/ngeo943>.